Three-dimensional MHD simulation of two coronal mass ejections' propagation and interaction using a successive magnetized plasma blobs model

F. Shen,[1] X. S. Feng,[1] Yuming Wang,[2] S. T. Wu,[3] W. B. Song,[1] J. P. Guo,[1] and Y. F. Zhou[1]

Received 18 February 2011; revised 7 June 2011; accepted 12 July 2011; published 24 September 2011.

[1] A three-dimensional (3-D), time-dependent, numerical magnetohydrodynamic (MHD) model is used to investigate the evolution and interaction of two coronal mass ejections (CMEs) in the nonhomogeneous ambient solar wind. The background solar wind is constructed on the basis of the self-consistent source surface with observed line of sight of magnetic field and density from the source surface of 2.5 R_s to Earth's orbit (215 R_s) and beyond. The two successive CMEs occurring on 28 March 2001 and forming a multiple magnetic cloud in interplanetary space are chosen as a test case, in which they are simulated by means of a two high-density, high-velocity, and high-temperature magnetized plasma blobs model, and are successively ejected into the nonhomogeneous background solar wind medium along different initial launch directions. The dynamical propagation and interaction of the two CMEs between 2.5 and 220 R_s are investigated. Our simulation results show that, although the two CMEs are separated by 10 h, the second CME is able to overtake the first one and cause compound interactions and an obvious acceleration of the shock. At the L1 point near Earth the two resultant magnetic clouds in our simulation are consistent with the observations by ACE. In this validation study we find that this 3-D MHD model, with the self-consistent source surface as the initial boundary condition and the magnetized plasma blob as the CME model, is able to reproduce and explain some of the general characters of the multiple magnetic clouds observed by satellite.

Citation: Shen, F., X. S. Feng, Y. Wang, S. T. Wu, W. B. Song, J. P. Guo, and Y. F. Zhou (2011), Three-dimensional MHD simulation of two coronal mass ejections' propagation and interaction using a successive magnetized plasma blobs model, *J. Geophys. Res.*, *116*, A09103, doi:10.1029/2011JA016584.

1. Introduction

[2] Coronal mass ejections (CMEs) and their interplanetary consequences (ICMEs) represent different aspects of the same phenomenon responsible for large nonrecurrent geomagnetic storms [*Gosling*, 1990]. Earth-directed CMEs usually take about 2–3 days to reach Earth's environment at 1 AU where they are observed in situ as ejecta. It is of great importance to understand the propagation of CMEs in the corona and their physical relationship to ejecta propagating through the interplanetary medium [*Wu et al.*, 1999, 2002]. Early Helios observations have shown that the ejecta can interact with one another, with shocks, and with corotating streamers. SOHO and WIND observations have revealed that CMEs cannibalize and deflect one another. CMEs are also accelerated and decelerated owing to their interaction with the solar wind [*Andrews and Howard*, 2001]. With the improvement of coronagraphic observations and the presence of the solar wind measurement in the outer heliosphere (Voyager, Ulysses), it is believed that successive ICMEs can merge with each other and form a compound structure, as mentioned formerly [e.g., *Burlaga et al.*, 2002; *Lugaz and Roussev*, 2010]. The same phenomenon also happens in the inner heliosphere, before CMEs reach Earth. When two or more ejections interact, they can form the well-known multiple ICME or magnetic cloud structure [*Wang et al.*, 2002, 2003]. These CMEs interactions result in different solar wind signatures as well as different geoeffectiveness as compared to isolated CME events.

[3] Numerical simulations, which yield the observed complexity, are useful to understand and determine the dynamical evolutionary processes of the CMEs interactions. To this end, scientists have developed various numerical models as reviewed by *Dryer* [2007] and *Feng et al.* [2011]. In the last 10 years, such numerical simulations have been

[1]SIGMA Weather Group, State Key Laboratory of Space Weather, Center for Space Science and Applied Research, Chinese Academy of Sciences, Beijing, China.
[2]School of Earth and Space Sciences, University of Science and Technology of China, Hefei, China.
[3]Center for Space Plasma and Aeronomic Research, University of Alabama in Huntsville, Huntsville, Alabama, USA.

0148-0227/11/2011JA016584

performed to reproduce the process of the CME-CME interaction and their interplanetary manifestations [*Wu et al.*, 2002, 2007; *Schmidt and Cargill*, 2004; *Wang et al.*, 2005; *Lugaz et al.*, 2005, 2007; *Hayashi et al.*, 2006; *Xiong et al.*, 2006a, 2006b, 2007, 2009; *Zhou and Feng*, 2008; *Odstrcil and Pizzo*, 2009]. Using a flux rope and streamer model, *Wu et al.* [2002] performed a two and a half dimensional (2.5-D) MHD simulation of CME and CMEs interaction in a bimodal solar wind from near the Sun to ~30 R_s, on the basis of the two CMEs interaction event recorded by SOHO/LASCO on 20 January 2001. *Schmidt and Cargill* [2004] studied the interaction of two CMEs in the similar region through 2.5-D MHD simulations, in which the scenarios with and without direct magnetic interactions between the flux ropes were comparatively analyzed.

[4] The event of multiple magnetic cloud (MultiMC) in interplanetary space on 31 March 2001, which caused the largest geomagnetic storm with $Dst = -387$ nT during the 23th solar maximum (2000–2001), was studied by many authors [*Wang et al.*, 2003, 2004, 2005; *Lugaz et al.*, 2005; *Farrugia et al.*, 2006]. This MultiMC structure was formed by the overtaking of successive CMEs recorded by SOHO/LASCO [*Wang et al.*, 2003]. Then, on the basis of this MultiMC event, *Wang et al.* [2005] used a 2.5-D MHD code to numerically study the formation and propagation of two identical CMEs, which were assumed to be initially separated by 12 h and radially ejected along the exact same direction, with speeds of 400 and 600 km/s. Their result implied that the travel time of a MultiMC structure was almost determined by the preceding slow cloud but they cannot simulate the associated shock owing to the high numerical dissipation in their code. In the same year, *Lugaz et al.* [2005] simulated the same MultiMC event by using a 3-D MHD code. In their study, two identical CMEs modeled as two 3-D magnetic flux ropes [*Manchester et al.*, 2004] were launched with the same radial direction, with the second one 10 h later than the first one. Their results show that the second CME catches up with the first one; the two shocks driven by the both CMEs merge and form a stronger, faster shock; and a first compressively heated cloud with a second overexpanded cloud could be distinguished at Earth.

[5] In those studies for the 28 March to 1 April 2001 MultiMC event [e.g., *Wang et al.*, 2005], the bimodal solar wind model was used for the preexisting solar wind, and the two CMEs were assumed to propagate in the same direction. A bimodal solar wind model may be suitable to reflect solar minimum conditions but this CMEs interaction event occurred near solar maximum. Moreover, SOHO/EIT observations showed that the two halo CMEs forming the MultiMC event originated from the solar surface source regions around N20E22 and N18E02 on 28 March 2001 [*Wang et al.*, 2003], which means that the two CMEs did not propagate along the same direction. The coupling of multiple CMEs from the same/different heliographic location of source region was defined as the direct/oblique collision by *Xiong et al.* [2006b]. Thus, the two CMEs interaction in the end of March 2001 should be better treated as an oblique collision than a direct collision.

[6] In the present paper, we employ a 3-D MHD code (COIN-TVD MHD model) with self-consistent source surface structures as initial boundary conditions [*Shen et al.*, 2007, 2011], which is derived from the observation of the solar magnetic field and K coronal brightness [*Wei et al.*, 2003]. The high-density, high-velocity and high-temperature magnetized plasma blob model [*Chané et al.* 2005, 2006, 2008; *Shen et al.*, 2011] is used for the initiation of the two halo CMEs observed by SOHO/LASCO on 28 March 2001. According to the observation, the centers of the two blobs are located at N20E22 and N18E02. The simulated background solar wind is presented in section 2, the simulation of the propagation and interaction of the 28 March to 1 April 2001 two CMEs event is given in section 3. Finally, a summary and concluding remarks are given in section 4.

2. Three-Dimensional MHD Simulation of Solar Wind Background for CR 1974

[7] The computational domain for this 3-D MHD simulation is a Sun-centered spherical coordinate system (r, θ, φ) with the r axis in the ecliptic plane. Earth (the L1 point) is located at $r = 215$ R_s (213 R_s), $\theta = 0°$, and $\varphi = 180°$. The computational domain covers $2.5\ R_s \le r \le 220\ R_s$; $-89° \le \theta \le 89°$ and $0° \le \varphi \le 360°$. The grid mesh is chosen to be $394(r) \times 89(\theta) \times 180\ (\varphi)$. The grid size is uniform in azimuth, with $\Delta\varphi = 2°$. The radial grid (r_i) and meridional grid (θ_j) are not uniform. In order to obtain a precise computational resolution, we choose for the radial grid: $r(1) = 2.5\ R_s$, $\Delta r(1) = s \times \mathrm{r}(1)$, $r(i) = r(i-1) + \Delta r(\mathrm{i}-1)$, $\Delta r(i) = s \times \mathrm{r}(i-1)$, where $s = \pi/200$ ($\pi = 3.1415926$) between 2.5 and 22 R_s, and $s = \pi/260$ between 22 and 220 R_s. The smallest grid cell on the source surface is ~0.04 R_s and the largest is ~2 R_s near 1 AU. For the meridional grid we choose $\Delta\theta$ (0°) = 1.0°, $\Delta\theta$ (−89°) = $\Delta\theta$ (89°) = 3.0°, with a constant increase in $\Delta\theta$ from $\theta = 0°$ to $\theta = \pm 89°$.

[8] The numerical 3-D MHD scheme used in the COIN-TVD MHD model is a modified Total Variation Diminishing/Lax-Friedrichs (TVD/LF) type scheme [*Feng et al.*, 2003, 2005; *Shen et al.*, 2007, 2009, 2011] with electric field modification method [*Tóth*, 2000] for the assurance of $\nabla \cdot \vec{B}$ 0. The time-dependent 3-D ideal MHD equations also include solar rotation and volumetric heating. The equations can be written in a spherical-component form at the inertial (nonrotating) reference frame, which was described in detail in our pervious paper [*Shen et al.*, 2007].

[9] The self-consistent source surface distribution is used as the initial boundary conditions at 2.5 R_s [*Wei et al.*, 2003; *Shen et al.*, 2007, 2010, 2011]. The initial conditions magnetic field (B_r, B_θ, B_φ) can be deduced from the photospheric magnetic field (B_r) with the model of horizontal current and current sheet (HCCS) [*Zhao and Hoeksema*, 1994] for CR 1974 according to an observation-based model of the background solar wind [*Xiang et al*., 2006; *Shen et al.*, 2007, 2010, 2011]. The initial coronal density (ρ) can be derived from the K coronal polarized brightness (pB) by MKIII the High-Altitude Observatory (HAO), following the solar wind density model [*Guhathakurta et al.*, 1996; *Xiang et al.*, 2006; *Shen et al.*, 2010]. And the other initial four parameters for v_r, v_θ, v_φ and T can be computed according to the initial density distribution and the self-consistent initial boundary conditions at the inner boundary [*Shen et al.*, 2007, 2010, 2011].

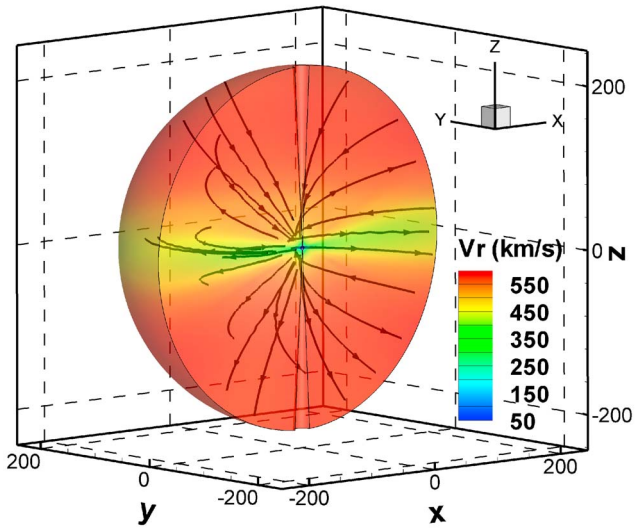

Figure 1. The calculated steady state 3-D magnetic field lines and radial velocity distribution from 2.5 to 220 R_s at 100 h. (Axis units given in R_s.)

[10] In order to reasonably accommodate the source surface distribution into our MHD model, the method of projected characteristics [*Nakagawa et al.*, 1987; *Wu and Wang*, 1987; *Hayashi*, 2005; *Wu et al.*, 2006; *Shen et al.*, 2011] is employed at the lower boundary (2.5 R_s). For the details about the method of projected characteristics, refer to *Wu et al.* [2006, Appendix]. At the outer boundary of 220 R_s, we employ a linear extrapolation. Because the solar wind is supersonic/Alfvénic at the outer boundary, this treatment is equivalent to a nonreflecting boundary.

[11] To save computation time and maintain simulation accuracy, we use the asynchronous and parallel time-marching method by using different local time steps (adapted to the local CFL condition) in the corona (2.5 to 22 R_s) and the heliosphere (22 to 220 R_s), and applying parallel computation in the r direction for this simulation [*Shen et al.*, 2009]. The simulation time of the background solar wind using the asynchronous method is <1/6 of that using the normal synchronous time-marching method without any influence on computation precision.

[12] The calculated steady state 3-D magnetic field topology and radial velocity distribution are shown in Figure 1. It takes ~100 h to reach the MHD equilibrium state. The well-known Archimedes' spiral lines are reproduced in Figure 1.

[13] Figure 2 shows the distributions of B_r, n, T and V_r in the corona (r = 22 R_s) and the heliosphere (r = 215 R_s) based on the asynchronous time-marching method. Profiles of the radial magnetic field (B_r), proton number density (n), temperature (T), and the radial velocity (v_r) at r = 22 R_s (corona) and r = 215 R_s (heliosphere) (meridional profiles at $\varphi = 180°$) are shown in Figures 2a–2d, respectively. The configurations in both the corona and the heliosphere display a dense, low-temperature and slow flow near the current sheet, while the sign of the radial magnetic fields are different at the two sides of the current sheet. These simulated features about the heliosphere are consistent with the Ulysses observation [*McComas et al.*, 2000, 2003, 2006].

3. Numerical Simulation of the Two CMEs Event on 28–30 March 2001

3.1. CME Initiation

[14] Detailed descriptions of the 28 March 2001 event have been reported by *Wang et al.* [2003, 2004]. For completeness we will summarize some of the highlights for this event.

[15] The first halo CME was visible in LASCO/C2 at 01:27 UT on 28 March 2001. The projected speed according to the LASCO CME catalog is 427 km/s. This CME was considered to be associated with a C5.6 X-ray flare which erupted from AR9401 (N20E22) at 01:29 UT. The second halo CME was visible in C2 at 12:50 UT on the same day. The projected speed is 519 km/s according to the LASCO CME catalog. An M4.3 X-ray flare beginning at 11:21 UT was detected accompanying this event, located in the AR9393 (N18E02). The interval of the two CMEs' initiation was 11.38 h. If their projected speeds were representative of the speeds along the Sun-Earth direction, the second CME was moving faster than the first one. Therefore, it could overtake the earlier one and form a MultiMC as was observed by ACE [*Wang et al.*, 2003]. On 31 March 2001, a very intense forward shock arrived at the L1 point (1.5×10^9 m from Earth sunward) at 00:20 UT on the basis the ACE spacecraft observation. Then, the first magnetic cloud was observed from 05:05 to 10:15 UT and the second one was observed during 12:35–21:40 UT. This MultiMC event caused the largest geomagnetic storm with *Dst* value of −387 nT during the 23th solar maximum (2000–2001) [*Wang et al.*, 2003].

[16] To simulate this two-CME event, two high-density, high-velocity and high-temperature magnetized plasma blobs are superimposed successively on a background steady state solar wind medium and a disturbed solar wind medium. The magnetized plasma blob model given by *Chané et al.* [2005, 2006, 2008] is a kind of very simple non force free flux rope model for CME initiation, which has relative simple type and can reproduce some features about the magnetic cloud; moreover, the best fit parameters of the CME initial state can be determined to get a relative close comparison with the ACE data at the L1 point. In our previous paper [*Shen et al.*, 2011], we used the magnetized plasma blob model to simulate the 4 April 2000 event, and get a relative close comparison with the ACE data at the L1 point. In the plasma blob model, the CME can be launched at a certain velocity, in a given direction and are further characterized by a given density, radial velocity, temperature, magnetic field strength and magnetic polarity. The initial CME magnetic field and the background wind magnetic field can have the same or the opposite polarity. It can be called as an inverse and a normal CME, as described by *Chané et al.* [2005, 2006].

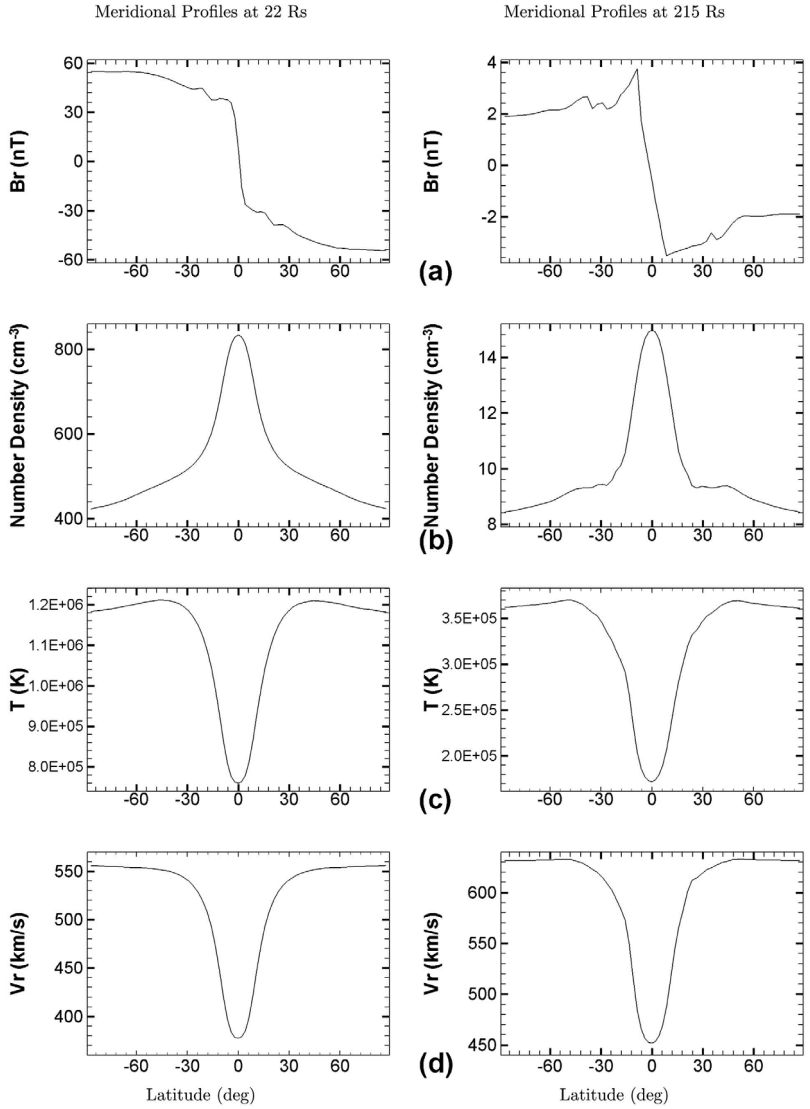

Figure 2. Profiles of (a) the radial magnetic field, (b) proton number density, (c) temperature, and (d) the radial velocity at $r = 22\ R_s$ (corona, left) and $r = 215\ R_s$ (heliosphere, right; meridional profiles at $\varphi = 180°$).

[17] The density, radial velocity and temperature profiles of the initial perturbation are defined as follows:

$$\begin{cases} \rho_{CME}(r,\theta,\varphi) = \frac{\rho_{\max}}{2}\left(1-\cos\left(\pi\frac{a_{cme}-a(r,\theta,\varphi)}{a_{cme}}\right)\right) \\ V_{CME}(r,\theta,\varphi) = \frac{v_{\max}}{2}\left(1-\cos\left(\pi\frac{a_{cme}-a(r,\theta,\varphi)}{a_{cme}}\right)\right) \\ T_{CME}(r,\theta,\varphi) = \frac{T_{\max}}{2}\left(1-\cos\left(\pi\frac{a_{cme}-a(r,\theta,\varphi)}{a_{cme}}\right)\right) \end{cases} \quad (1)$$

where, a_{cme} is the radius of the initial plasma blob, $a(r, \theta, \varphi)$ denotes the distance from the center of the initial plasma blob, which can be written as $a(r,\theta,\phi) = \sqrt{r^2 + r_{cme}^2 - 2rr_{cme}[\sin\theta\sin\theta_{cme}\cos(\phi-\phi_{cme}) + \cos\theta\cos\theta_{cme}]}$, and $(r_{cme}, \theta_{cme}, \varphi_{cme})$ is the position of the initial blob center. Here $\rho_{\max}$, $v_{\max}$ and $T_{\max}$ are the maximum density, radial velocity and temperature in the plasma bubble added on top of the background solar wind, respectively.

[18] The initial magnetic field of the perturbation in r and θ direction can be defined as [*Shen et al.*, 2011]

$$\begin{cases} B_{r_{CME}}(r,\theta,\varphi) = -\dfrac{1}{r^2\sin\theta}\dfrac{\partial\psi(r,\theta,\varphi)}{\partial\theta} \\ B_{\theta_{CME}}(r,\theta,\varphi) = \dfrac{1}{r\sin\theta}\dfrac{\partial\psi(r,\theta,\varphi)}{\partial r} \end{cases} \quad (2)$$

where

$$\psi(r,\theta,\varphi) = \psi_0\left(a(r,\theta,\varphi) - \frac{a_{CME}}{2\pi}\sin\left(\frac{2\pi a(r,\theta,\varphi)}{a_{CME}}\right)\right) \quad (3)$$

is the magnetic flux function.

[19] This initial perturbation will be given by the following relation:

$$\begin{cases} \rho = \rho_0 + \rho_{CME}(r,\theta,\varphi) \\ v_r = v_{r0} + V_{CME}(r,\theta,\varphi) \\ T = T_0 + T_{CME}(r,\theta,\varphi) \\ B_r = B_{r0} + B_{rCME}(r,\theta,\varphi) \\ B_\theta = B_{\theta 0} + B_{\theta CME}(r,\theta,\varphi) \end{cases} \quad (4)$$

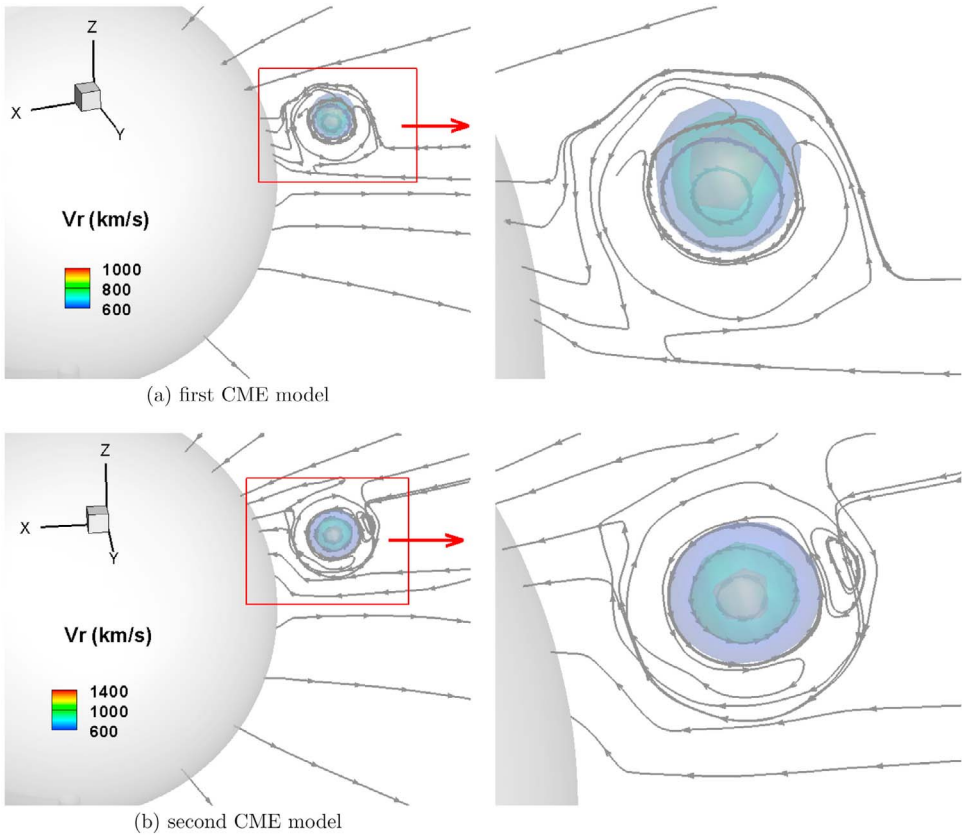

Figure 3. Three-dimensional views of the isosurface of the radial velocity v_r and the initial magnetic field lines of the CME initialization for (a) the first CME and (b) the second CME, including zooming in on the plasma blob.

where ρ_0, v_{r0}, T_0, B_{r0} and $B_{\theta 0}$ are the background values of the density, radial velocity, temperature, magnetic field in radial direction and in meridional direction calculated in section 2.

[20] In our simulation, the radius of the two plasma blobs $a_{\rm cme}$ is set as 0.5 R_s and the center of the initial plasma blobs is situated at 3.5 R_s. The second plasma blob is initiated 10 h after the launch of the first one. The other parameters are given as following:

[21] 1. For the first CME (CME1), the initial plasma blob is launched in direction of θcme = 20° and φcme = 158° (N20E22 event); the maximum density ($\rho_{\rm max}$), radial velocity ($v_{\rm max}$) and temperature ($T_{\rm max}$) are set as 1.2 × 10^9 cm^{-3}, 1200 km/s and 4 × 10^6K, respectively; ψ_0 is set as 2.0 to obtain the initial maximum magnetic field strength as ~6 × 10^5 nT;

[22] 2. For the second CME (CME2), the initial plasma blob is launched in direction of θcme = 18° and φcme = 178° (N18E02 event); the maximum density ($\rho_{\rm max}$), radial velocity ($v_{\rm max}$) and temperature ($T_{\rm max}$) are set as 1.5 × 10^9 cm^{-3}, 1500 km/s and 5 × 10^6K, respectively; ψ_0 is set as −2.4 to obtain the initial maximum magnetic field strength as ~8 × 10^5 nT, with an inverse magnetic polarity compared with CME1.

[23] The parameters of the magnetized plasma blob are chosen to agree with the observed values of initial latitude, longitude and approximate speed of the two CMEs (assuming the $v_{\rm ave}$ of the plasma blob approximately equal to 1/3 $v_{\rm max}$) from SOHO/LASCO, the maximum of the shock speed, numerical density and the changing mode of B_z (N-S-N-S) at the L1 point observed by ACE as the best fit as possible. This initiation model will yield the driving force to launch a CME. The introduction of the additional heating by raising the temperature of the plasma blob can generate the driving force to launch a CME, since the pressure force is calculated from $p = \rho RT$, which was also mentioned in our previous paper [*Shen et al.*, 2011].

[24] Figure 3 displays the 3-D intuitive views of the isosurfaces with three values of the radial velocity v_r and the initial magnetic field lines of CME1 (Figure 3a) and CME2 (Figure 3b) initialization on the background solar wind, including zooming in on the plasma blob. It should be pointed out that to emphasize the initial plasma blob, we only shows three kinds of color corresponding to three levels of the isosurface of the radial velocity v_r, which are v_r = 1000, 800, 600 km/s in Figure 3a and v_r = 1400, 1000, 600 km/s in Figure 3b, without showing the other levels of color contours. Figures 3a and 3b show that the maximum value of the radial velocity appeared at the center of the initial plasma blob in the two CMEs initialization, and the magnetic field of CME2 has initially the inverse polarity compared with CME1.

3.2. Dynamical Evolution, Overtaking, and Interaction of the Two CMEs

[25] In this section, the simulation results are presented. To identify the shock front, we use the value of the relative

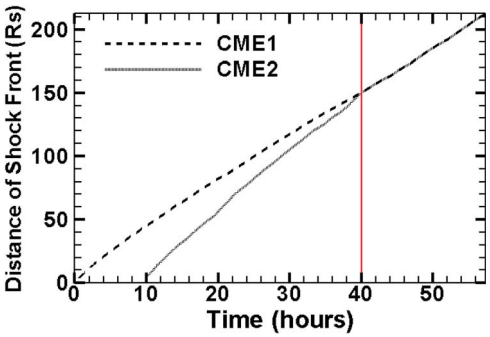

Figure 4. Comparison of the shock front heliocentric distance between the first CME (dashed line) and the second CME (solid line).

density $((\rho - \rho_o)/\rho_o)$ being 2.0 as the criterion to identify the position of the shock front. Then we define the distance of the shock front by using the maximum value of the heliocentric distance in the shock front plane. Figure 4 shows a time-height plot of the shock front distance of the two CMEs from $t = 0$ to 57.3 h. The second eruption is initiated 10 h after the launch of the first one, at which time the distance of the CME1's shock front is at 45.3 R_s.

[26] Figures 5 and 6 show the 3-D propagation of the simulated CMEs at 40 min (Figures 5a and 6a), 5 h (Figures 5b and 6b), 10 h 40 min (40 min after CME2 launched) (Figures 5c and 6c), 20 h (Figures 5d and 6d), 32 h (Figures 5e and 6e), 40 h (Figures 5f and 6f), 50 h (Figures 5g and 6g) and 60 h (Figures 5h and 6h) after the launch of CME1. Figure 5 represents the relative density $((\rho - \rho_o)/\rho_o)$ and magnetic field lines, and Figure 6 shows the radial velocity and magnetic field lines. The magnetic field topology is represented by the rod-shaped magenta lines in both Figures 5 and 6. Because the initial heliolatitudes of the two CMEs are similar (θ = 20° and 18°), a 2-D distribution of the relative density at a constant latitude angle of 18° is given in Figure 7 to provide another view of the two CMEs at t = 30 h (Figure 7a), 32 h (Figure 7b), 36 h (Figure 7c) and 40 h (Figure 7d).

[27] The shock fronts with a high velocity and relatively high density are clearly visible in Figures 5, 6, and 7. At time t = 40 min, the flux rope of CME1 still remain an almost circular shape, but is quickly stretched to a pancake shape after t = 5 h. The same thing also happens to CME2. At t = 20 h, the distance between the shock fronts of the two CMEs is 25.7 R_s and the two flux ropes get closer. At t = 32 h, the shock front of CME2 reaches the trailing edge of CME1. Then from 32–40 h the shock of CME2 penetrates through the body of CME1. At time t = 39 h, the two shock fronts are only 2.37 R_s apart, and from time t = 40 h, the two shocks begin to merge to a stronger combined shock, seen from Figures 4 and 7 and from Figures 5e, 5f, 6e, and 6f. In Figures 5e–5h and 6e–6h, after time t = 32 h, the flux rope of CME2 with relative low density and high velocity overtakes the flux rope of CME1, and the oblique collision occurs between the two flux ropes. It induces obvious deformation

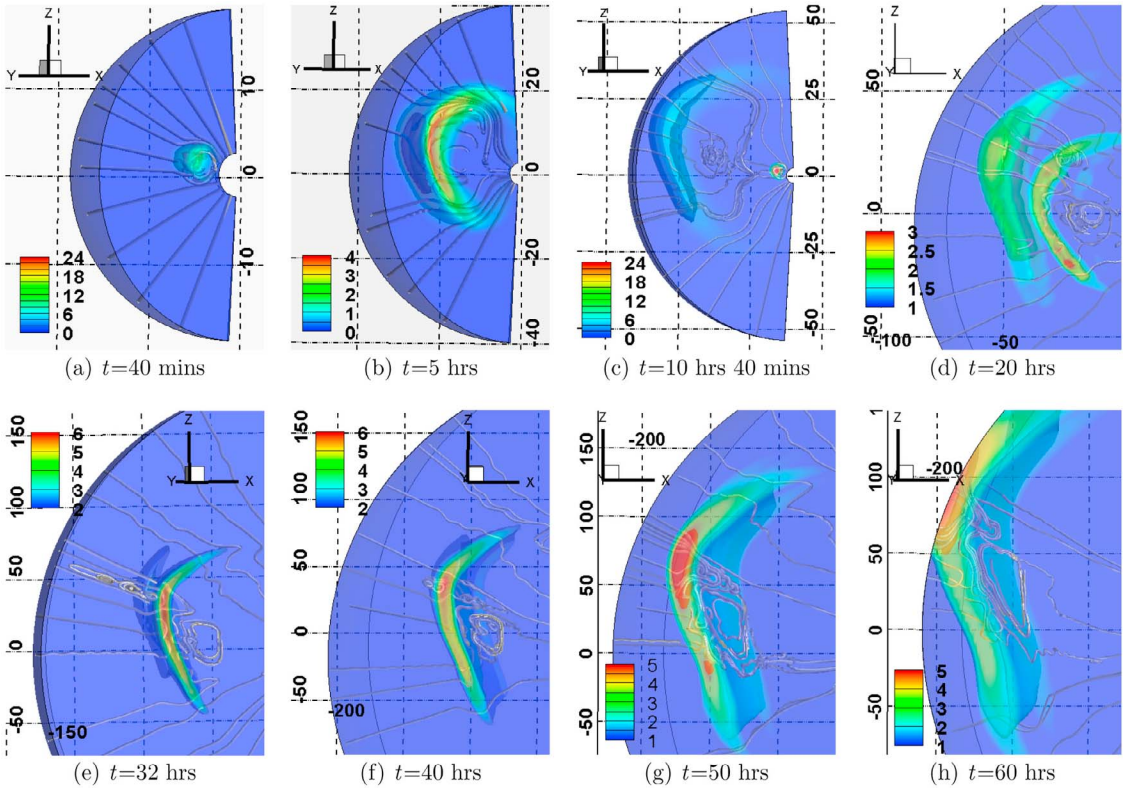

Figure 5. Three-dimensional representation of the CMEs (140° < φ < 180°) shown (a) 40 min, (b) 5 h, (c) 10 h 40 min (40 min after the second CME launched), (d) 20 h, (e) 32 h, (f) 40 h, (g) 50 h, and (h) 60 h after the first CME initiation. The solid rod-shaped lines are magnetic field lines, and the color codes represent the relative density $((\rho - \rho_0)/\rho_0)$. (Axis units given in R_s.)

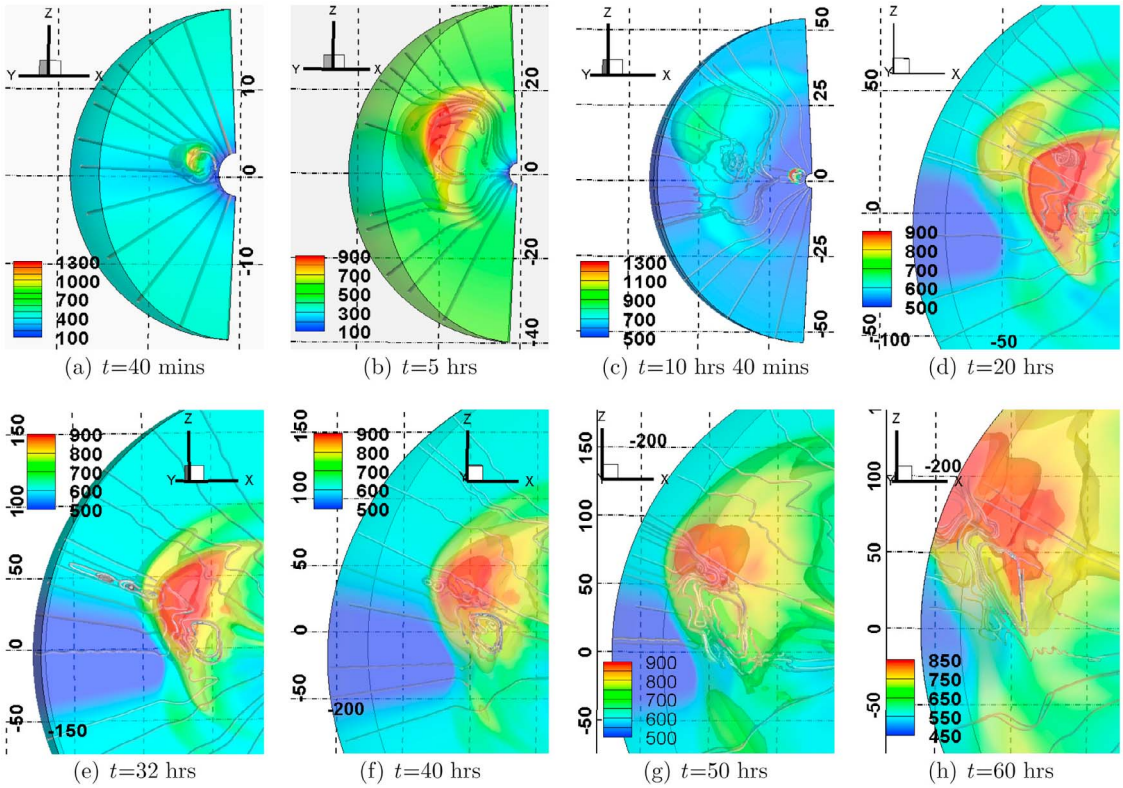

Figure 6. Three-dimensional representation of the CMEs ($140° < \varphi < 180°$) shown (a) 40 min, (b) 5 h, (c) 10 h 40 min (40 min after the second CME launched), (d) 20 h, (e) 32 h, (f) 40 h, (g) 50 h, and (h) 60 h after the first CME initiation. The solid rod-shaped lines are magnetic field lines, and the color codes represent the radial velocity magnitude. (Axis units given in R_s.)

and compression of the two flux ropes, and the second flux rope develops its shape from circular-like structure to a flat structure. However, there are not coherent spiral-shaped magnetic field lines in Figures 5 and 6, which can be explained by that the absence of an initial axial component B_φ may destabilize the imposed magnetic field.

[28] To study the interaction between the two CMEs, we make a comparison of the simulation results among three different cases: double CMEs, CME1 only and CME2 only, with other conditions being the same. Figures 8a and 8b show the comparison results of the temporal evolution of the heliocentric distances of the shock fronts from near the Sun to 213 R_s for CME1 and CME2, respectively. In Figures 8a and 8b the shock fronts of CME1 and CME2 in the interaction case moves faster than those in noninteraction case. In Figure 8a the influence of CME2 to the moving speed of the shock front of CME1 primarily happens after time $t = 40$ h, when the shock of CME2 overtakes the shock of CME1 and merging into one combined shock. While in Figure 8b the difference of the two curves happens much earlier than in Figure 8a. After time about $t = 10$ h, the heliocentric distance of the shock front of CME2 in the interaction case increases more quickly than that of only CME2 case. This is probably because, when CME1 propagates into the background solar wind, it removes some of the background's mass. Associated with the propagation of the CME, there is as well a disruption of the solar wind, especially of the background magnetic field. As a consequence, CME2 does not propagate into the background solar wind, but into a disturbed medium, less dense, faster and more magnetized. This kind of analysis was also made by *Lugaz et al.* [2005].

[29] Figure 9 plots the velocity (v; Figure 9a) and z component magnetic field (B_z; Figure 9b) at the L1 point from time $t = 40$ h to 100 h of the double-CME case (black line), of only CME1 (red line), of only CME2 (initial time $t = 0$ h, to be compared with only CME1 case) (green line) and of only CME2 shifted by 10 h (initial time $t = 10$ h, to be compared with double-CME case) (blue line). From comparing the red line and green line of Figure 9a, the arrival time of the shock at the L1 point is 70.4 h and 61.9 h of the only CME1 case and only CME2 case after the CME initiation, respectively, which demonstrates that the initial velocity of the CMEs can obviously influence the arrival time of the shock at the L1 point. Meanwhile, we can compare the arrival time at the L1 point of the shock using two CMEs initiation (black line) with using only one CME initiation (red line and blue line), since the exact same parameters are used in both cases to generate the CME. We notice that the shock arriving at the L1 point ~67.4 h after the launch of CME1, whereas in the case without interaction, the shock arrives at the L1 point 70.4 h for only CME1 case and 71.9 h for only CME2 case. So the arrival time of the shock with two CMEs interaction is the shortest one among the three cases, which is also consistent with the result of Figure 8. At the shock, the solar wind speed jumps from

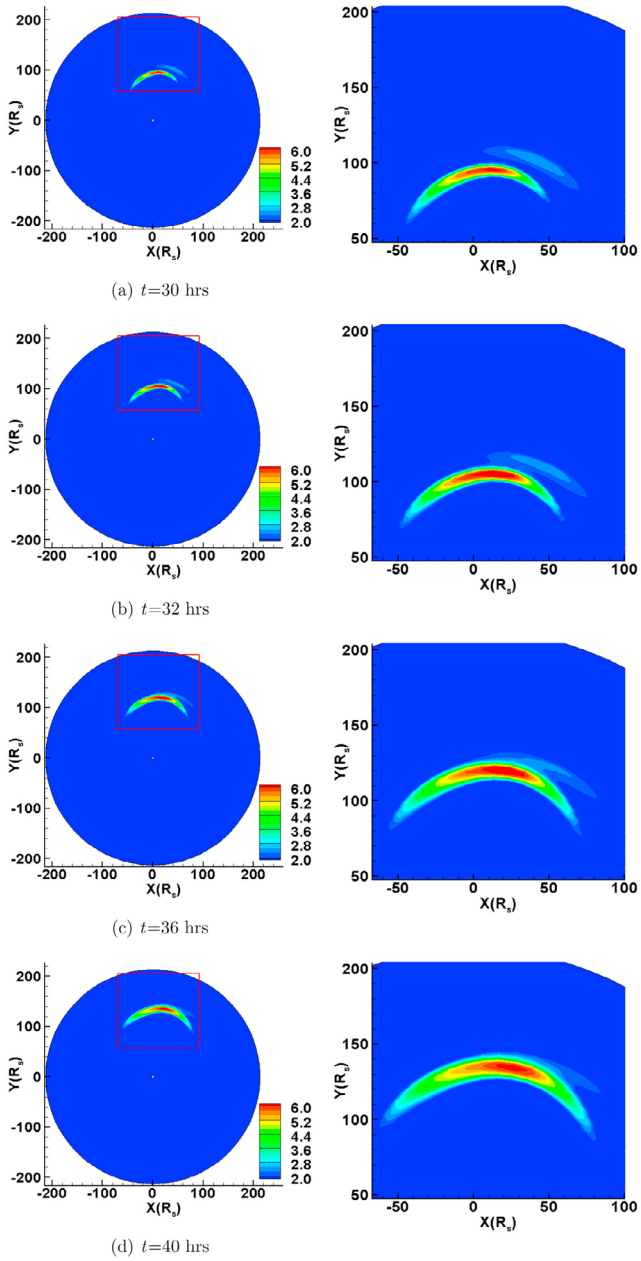

Figure 7. Evolution of the two-dimensional relative density $((\rho - \rho_0)/\rho_0)$ contours of the constant latitude angle of $\theta = 18°$ at four consecutive times. (Axis units given in R_s.)

about 457 km/s to over 650 km/s for two CMEs interaction case, to about 550 km/s for only CME1 case and to about 610 km/s for only CME2 case, respectively, which indicates that the shock of the two CMEs merges into one stronger combined shock.

[30] In Figure 9b, for the z component of the magnetic field, the profiles for the three cases at the L1 point are different: (1) becoming northward first, then changing to southward, later changing to northward again, and finally tuning southward for a long time for two CMEs interaction case; (2) becoming northward first, then changing to southward, and finally turning to near 0 for only CME1 case; and (3) becoming southward first, then changing to northward, later changing to southward slightly, and finally turning to near 0 for only CME2 case. The maximum of the south component of magnetic field, B_s, is about 34 nT for two CMEs interaction case, while only about 5 nT for only CME1 case and about 13 nT for only CME2 case. The fact that the large duration of a strong B_s appearing in the double-CME interaction cases, does not appear in the only CME1 case or the only CME2 case suggests the importance of the interaction between two CMEs in causing major geomagnetic storms.

3.3. Properties of the Simulated CMEs at L1 Point and Comparison With ACE Data

[31] Figure 10 shows the comparison of the computed plasma and field parameters at the L1 point in Figure 10b with the observed MultiMC of 31 March to 1 April 2001 shown in Figure 10a. Figure 10 depicts the plots of total, z component magnetic field in GSE coordinate system, number density, temperature, velocity and plasma β at the L1 point. At the L1 point, the two flux ropes have evolved to show some of the characteristics commonly associated with MultiMC, namely two high magnetic field strength regions separated by a region of increased β, smooth variation of the magnetic field in each cloud, a shorter duration of the first cloud compare to the second one, low proton density and temperature in both clouds and a high-velocity profile [*Wang et al.*, 2003; *Lugaz et al.*, 2005].

[32] As seen in Figure 10b, the simulated shock reaches L1 at DOY of 89.86, marked with the blue vertical solid line, and the two magnetic clouds are preceded by a very strong shock with high density, temperature and velocity. The first compressed magnetic cloud (MC1) arrives at L1 during DOY of 90.22–90.40, marked with red vertical dashed line, and after a short time, the second overexpanded magnetic cloud (MC2) reaches L1 from DOY of 90.49, marked with green vertical dashed line. As the shock passes L1, the density increases from 16 cm^{-3} to 67 cm^{-3}, the temperature increases by a factor of over two and the velocity jumps from about 457 km/s to over 650 km/s. The velocity first decreases slightly behind the shock, but then increases again to a higher value of ~700 km/s in the MC2 than in the MC1. This obvious increase in velocity in the rear part of plasma is specific to this model of CME interaction, and was not found in only CME1 or only CME2 case, as seen from Figure 9a. At the sheath and MC1, the density drops from over 60 cm^{-3} to ~5 cm^{-3} and the temperature decreases from ~4 × 10^5 K to ~1.6 × 10^5 K. In MC2, both the density and temperature remain the relative low values of 4–6 cm^{-3} and 1.5 × 10^5–2 × 10^5 K, respectively, and the velocity remains relative high value of 680–740 km/s.

[33] The maximum magnetic field strength of 46 nT is obtained in the MC1 at DOY of 90.35, 12 h after the shock's arrival. In the connection region between MC1 and MC2, the magnetic field reaches a minimum value of 6.5 nT. The MC2 has a maximum magnetic field strength of 26.3 nT. As seen from Figures 9b and 10b, when the first flux rope arrives at the L1 point, B_z turns northward for about 8 h reaching a maximum value of 11.5 nT. Then, B_z smoothly rotates southward to reach a minimum value of −34 nT in MC1, and the magnetic field remains southward for 3.7 h. As the second flux rope passes L1, the magnetic field turns

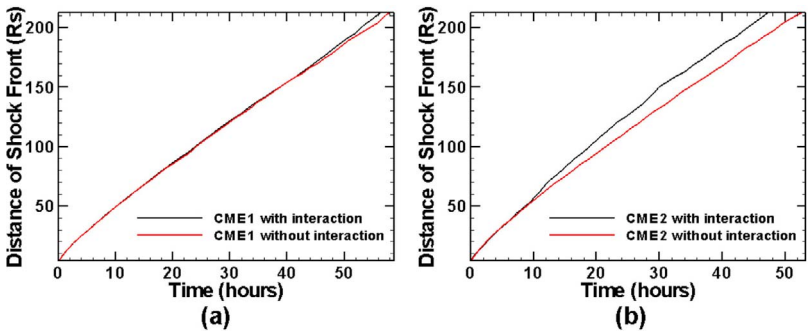

Figure 8. (a) Temporal evolution of shock front distance of the first CME with (black line) and without (red line) interaction with the second CME and (b) temporal evolution of shock front distance of the second CME with (black line) and without (red line) interaction with the first CME. For the black line in Figure 8b the time reference has been shifted by 10 h so that time $t = 0$ h corresponds to the initiation of the second CME.

to northward again for 3.4 h, reaching a maximum value of 16.8 nT, and then rotates southward for more than 16 h, reaching a minimum value of −12.5 nT. In the connection region between MC1 and MC2, the value of plasma β increases by a factor of ~17, corresponding to the low magnetic field. Such high-β interaction regions were also described by *Wang et al.* [2003] for three different MultiMC events in March–April 2001 and by *Lugaz et al.* [2005] for simulating this 28 March 2001 MultiMC event.

[34] Comparing our simulation result with ACE data, we find that in spite of the simple CME model used, our simulation is in good qualitative agreement with the data. The two MCs are preceded by a very strong shock with high density, temperature and velocity. The maximum values of the velocity and density almost display realistic values of over 700 km/s and 67 cm^{-3}, respectively. The transit time of MC1 from DOY of 90.22 to 90.40, and the start time of MC2 of DOY of 90.49 are approximately reproduced. The density, temperature and plasma β in the two MCs remain relative low value of almost below 20 cm^{-3}, 2×10^5 K and around 0.1, respectively, and the velocity in the two MCs has relative high value of 600–700 km/s, which are consistent with the values of density, temperature and velocity in MC1 and MC2 of observational data. The two MCs are separated by a region with a relative large β ($\beta_{max} > 1$, while around 0.1 in the clouds) and low magnetic field strength ($|B|_{min} < 10$ nT compared with values larger than 20 nT in the clouds). For the z component of the magnetic field, the simulated and measured profiles at the L1 point are similar, becoming northward first, then changing to southward, later changing to northward again, and finally turning southward. And the southward component of the magnetic field reaches a maximum value of 34 nT in MC1 and remains southward for a long time, which lead to a peak value of *Dst* of −387 nT [*Wang et al.*, 2003].

[35] Some quantitative disagreement between our simulation and reality is to be expected. The shock center characterized by the maximum value of the velocity arrives 3.6 h earlier in the simulation. The maximum value of the magnetic field strength and temperature in the simulation in only ~64% and ~50% of the ACE data, respectively. An obvious increase in magnetic field strength at the shock is absent and the magnetic field is weak in the simulated sheath, compared with the observational data. The simulated velocity of MC2 is higher than the measured data. The relative high temperature and density in the connection region between the two MCs aren't attained in the simulated profile, but can be seen in the measured profile. So the simulated maximum value of the plasma β in the connection region is much lower than the observational data.

[36] One limit causing the inconsistency is that our present model, like many others already mentioned, is only a

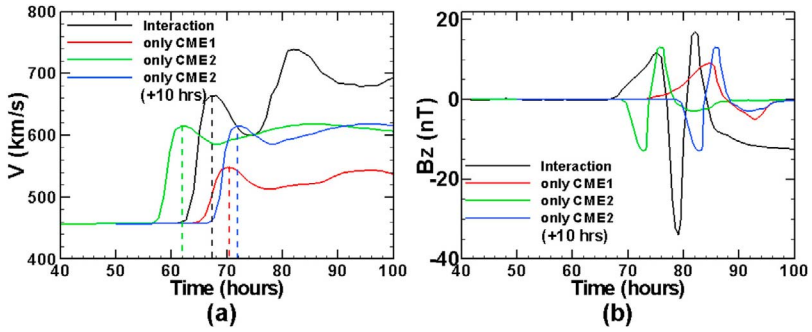

Figure 9. Temporal evolution of (a) velocity (v) and (b) z component magnetic field (B_z) at the L1 point of the double-CME case (black line), only the first CME (red line), only the second CME (initial time $t = 0$ h, to be compared with only the first CME case) (green line), and only the second CME shifted by 10 h (initial time $t = 10$ h, to be compared with double-CME case) (blue line).

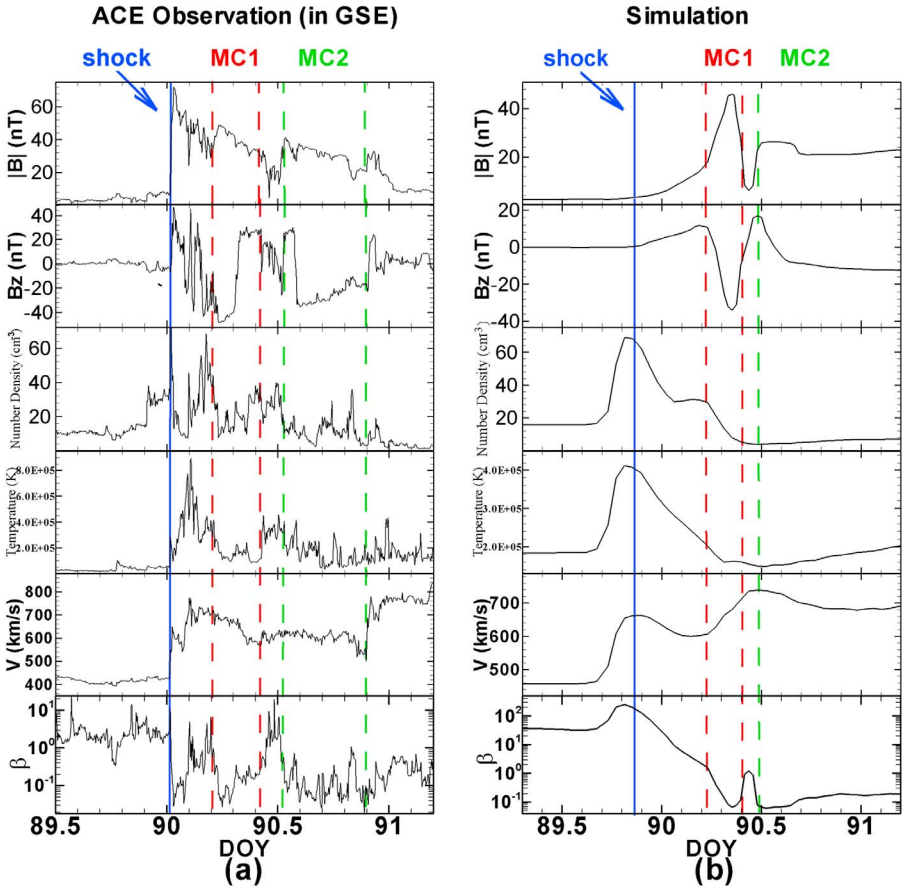

Figure 10. A comparison of the MHD simulation of the magnetic field and plasma parameters with the measured (ACE spacecraft) magnetic field and solar wind parameters at the L1 point in 2001. (a) Measured parameters by ACE, top to bottom: magnetic field strength $|B|$ (nT), B_z (nT) at GSE coordinate system, proton density (cm^{-3}), proton temperature (K), velocity (km/s), and plasma β. (b) Simulation parameters, top to bottom: magnetic field strength $|B|$ (nT), B_z (nT) at GSE coordinate system, number density (cm^{-3}), plasma temperature (K), velocity (km/s), and plasma β. The blue vertical solid lines indicate the arrival time at L1 of the shock, the red vertical dashed lines denote the beginning and ending of the first MC, and the green vertical dashed line denotes the beginning of the second MC.

single-fluid (proton) model, which cannot account for the high electron temperature in the CMEs and the anticorrelation between the electron temperature and density. The magnetic field by our model is always week compared to observations, which is also a result of the initial synoptic magnetic field being too weak at the poles. Meanwhile, the absence of an initial axial component B_φ may destabilize the flux rope and make it more prone to being deformed and incoherent, and can also influence other parameters, such as the mismatch of the higher velocity in MC2, the lower-density and lower-plasma β between the clouds, compared with the observation data. Moreover, there exist two other extremely important and still unsolved limits as pointed out by *Dryer* [1998, 2007] and now realized by many other modelers [*Fry et al.*, 2001; *Odstrcil et al.*, 2004; *Feng et al.*, 2011]. One is the uncertainty of the initial realistic solar wind and interplanetary magnetic field (IMF) background conditions, and the other is the uncertainty of the appropriate solar observations used to "mimic" solar flare/filament and CME initiation. To some extent, our establishment of using more observational data such as photospheric magnetic fields by SOHO/MDI and the brightness recorded in SOHO/LASCO to constrain the model is an attempt to reduce the uncertainty of the initial realistic solar wind. But, how to "mimic" solar flare/filament and CME initiation based on the solar observations is a challenge.

[37] We believe that more solar and interplanetary observations will be able to minimize these uncertainties. For example, the recently launched Solar Dynamic Observatory (SDO) will help us understand the Sun's magnetic changes. SDO will tell us more about how the magnetic field is generated and structured, and how the stored magnetic energy is released into the heliosphere and geospace. STEREO observations can provide new insights into the 3-D structure of CMEs and their evolution in the heliosphere which can directly be compared with existing models and simulations. Comprehensive data and analysis with multiple spacecraft (such as SDO, STEREO, SOHO, ACE, WIND, or other future missions) will probably help us develop the ability of including physically realistic coronal heating modules into 3-D MHD codes, improve the determination of the structure of the ambient solar wind, and further

numerically characterize the 3-D propagation of CMEs through the heliosphere, as mentioned by *Feng et al.* [2010, 2011].

4. Summary and Concluding Remarks

[38] We have used a three-dimensional time-dependent, numerical MHD model, together with an asynchronous and parallel time-marching method by *Shen et al.* [2009] to investigate large-scale background solar wind structures, and the propagation and interaction of two CMEs evolution, with its shock wave in a nonhomogeneous background solar wind flow. This background solar wind is derived from the observed photospheric magnetic field and density at the source surface.

[39] Using an asynchronous and parallel time-marching method, we first present the background solar wind from the source surface of 2.5 R_s to Earth's orbit (215 R_s) and beyond. In this simulation, we apply a self-consistent source surface structure as the initial boundary condition, and the projected normal characteristic method [*Nakagawa et al.*, 1987; *Wu and Wang*, 1987] to deal with the boundary condition at inner boundary. Our numerical results of the background solar wind are qualitatively consistent with observations results given by Ulysses.

[40] We then investigated the propagation and interaction of two CMEs with the background solar wind flow between 2.5 and 220 R_s. The two CMEs are simulated by means of two high-density, high-velocity and high-temperature magnetized plasma blob models, which are superimposed successively on a background steady state solar wind medium and a disturbed solar wind medium with different initial launch direction. We chose two successive halo-CMEs event of 28 March 2001 as our test case because of the abundant data available from the SOHO/LASCO and ACE spacecrafts. The initial parameters are chosen to agree with the observed values of initial latitude, longitude and approximate speed of the two CMEs from SOHO/LASCO, the maximum of the shock speed, numerical density and the changing mode of B_z (N-S-N-S) at the L1 point observed by ACE as the best fit as possible.

[41] The numerical simulation results of the 28 March to 1 April 2001 CME propagation, overtaking and interaction are shown in Figures 4–7. Figures 4–7 clearly show that a shock front with a high velocity and relatively high density is clearly visible, and the high-velocity and high-plasma density build up in front of the flux rope. From 32 h after CME1 launched, the flux rope structure with relative low density and high velocity following the shock of CME2 overtakes the flux rope of CME1, and the oblique collision occurs between the two flux ropes, which induces obvious deformation of the two flux ropes. At 40 h, the shock of CME2 merges with that of CME1, forming a stronger combined shock. To study the interaction between the two CMEs, we make a comparison of the simulation result among two CMEs case, only CME1 and only CME2, with other conditions being the same, as seen from Figures 8 and 9. It can be demonstrated that because of the interaction between the two successive CMEs, the arrival time of the shock at heliocentric distance of 213 R_s with two CMEs interaction is the shortest one among the three cases, and the maximum values of the velocity and southward B_z with two CMEs interaction are also the highest among the three cases. The large duration of a strong southward B_z of the two CMEs interaction case may lead to an increased geoeffectiveness.

[42] When the two CMEs evolve to the compound structure of MultiMC reaching the L1 point, its physical parameters (Figure 10) resembled the observations of the MultiMC recorded by the ACE spacecraft. Our simulation is in good qualitative agreement with the data as the following aspect: (1) the compressed MC1 and overexpanded MC2 are preceded by a very strong shock with high density, temperature and velocity; (2) the maximum values of the velocity, density, the transit time of MC1 and the start time of MC2 almost display realistic values; (3) the density, temperature and plasma β in the two MCs remain relative low value, and the velocity in the two MCs has relative high value; (4) the two MCs are separated by a region with a relative large β and low magnetic field strength; and (5) the simulated and measured profiles of B_z at the L1 point are similar, becoming northward first, then changing to southward, later changing to northward again, and finally tuning southward. The z component of the magnetic field is the most important parameter in predicting the intensity of a magnetic storm.

[43] The magnetized plasma blob model we used is a kind of very simple flux rope model for CME initiation, which has relative simple type and can reproduce some features about the magnetic cloud; moreover, the best fit parameters of the CME initial state can be determined to get a relative close comparison with the ACE data at the L1 point. It is the first time to use this magnetized plasma blob model to simulate the propagation and interaction of two CMEs evolution.

[44] While there still exist limitations in our model, such as (1) the absence of an initial axial component B_φ in the initial magnetic plasma blob model; (2) the weakness of initial polar magnetic field; (3) a single-fluid (proton) model; (4) the uncertainty of the initial realistic solar wind and IMF background conditions; and (5) the simplified assumption of solar flare/filament and CME initiation. In spite of these limitations, our 3-D MHD model, with the self-consistent source surface as initial boundary conditions and the magnetized plasma blob as CMEs model, is able to simulate the propagation, overtaking and the interaction of the two ICMEs, reproduce and explain some of the general characters of the multiple magnetic clouds observed in satellite data.

[45] **Acknowledgments.** This work is jointly supported by National Natural Science Foundation of China (41174150, 41031066, 41074121, 40921063, 40874077, 40890162 and 40874091), the Specialized Research Fund for State Key Laboratories and the Public science and technology research funds projects of ocean (201005017). Y. Wang is supported by 973 Key Project 2011CB811403. S. T. Wu is supported by AFOSR grant FA9550-07-1-0468, NSF grant ATM-0754378, and NSO/AURA grant C-10569A, which is a subaward of NSF Award 0132798. We thank the SOHO/LASCO team for letting us use their data. SOHO is a mission of international collaboration between ESA and NASA. The Wilcox Solar Observatory (WSO) data used in this study were obtained via the Web site http://wso.stanford.edu/synopticl.html for CR 1974. The WSO is currently supported by NASA. We also thank ACE Science Center (ASC; http://www.srl.caltech.edu/ACE/ASC/), from which we downloaded the hourly average solar wind data by ACE. The numerical calculation was completed on our SIGMA Cluster computing system. We are very grateful to our anonymous reviewers for the constructive and helpful comments.

[46] Philippa Browning thanks the reviewers for their assistance in evaluating this paper.

References

Andrews, M. D., and R. A. Howard (2001), A two-type classification of LASCO coronal mass ejections, *Space Sci. Rev.*, *95*, 147–163, doi:10.1023/A:1005284316619.

Burlaga, L. F., S. P. Plunkett, and O. C. St. Cyr (2002), Successive CMEs and complex ejecta, *J. Geophys. Res.*, *107*(A10), 1266, doi:10.1029/2001JA000255.

Chané, E., C. Jacobs, B. Van der Holst, S. Poedts, and D. Kimpe (2005), On the effect of the initial magnetic polarity and of the background wind on the evolution of CME shocks, *Astron. Astrophys.*, *432*, 331–339, doi:10.1051/0004-6361:20042005.

Chané, E., B. Van der Holst, C. Jacobs, S. Poedts, and D. Kimpe (2006), Inverse and normal coronal mass ejections: Evolution up to 1 AU, *Astron. Astrophys.*, *447*, 727–733, doi:10.1051/0004-6361:20053802.

Chané, E., S. Poedts, and B. Van der Holst (2008), On the effect of the initial magnetic polarity and of the background wind on the evolution of CME shocks, *Astron. Astrophys.*, *492*, L29–L32.

Dryer, M. (1998), Multi-dimensional MHD simulation of solar-generated disturbances: Space weather forecasting of geomagnetic storms, *AIAA J.*, *36*, 365–370, doi:10.2514/2.405.

Dryer, M. (2007), Space weather simulation in 3D MHD from the Sun to the Earth and beyond to 100AU: A modeler's perspective of the present state of the art, *Asian J. Phys.*, *16*, 97–121.

Farrugia, C. J., V. K. Jordanova, M. F. Thomsen, G. Lu, S. W. H. Cowley, and K. W. Ogilvie (2006), A two-ejecta event associated with a two-step geomagnetic storm, *J. Geophys. Res.*, *111*, A11104, doi:10.1029/2006JA011893.

Feng, X., et al. (2003), A class of two-step TVD MacCormack type numerical scheme for MHD equations, Chin. *J. Space Sci.*, *23*, 401–412.

Feng, X., et al. (2005), A comparative study on 3-D solar wind structure observed by Ulysses and MHD simulation, *Chin. Sci. Bull.*, *50*, 672–678, doi:10.1360/982004-293.

Feng, X., C. Xiang, S. T. Wu, Y. Zhou, and D. Zhong (2010), Three-dimensional solar wind modeling from the sun to Earth by a SIP-CESE MHD model with a six-component grid, *Astrophys. J.*, *723*, 300–319, doi:10.1088/0004-637X/723/1/300.

Feng, X. S., C. Q. Xiang, and D. K. Zhong (2011), The state-of-art of three-dimensional numerical study for corona-interplanetary process of solar storms (in Chinese), *Sci. Sin. Terrae*, *41*, 1–28.

Fry, C. D., W. Sun, C. S. Deehr, M. Dryer, Z. Smith, S.-I. Akasofu, M. Tokumaru, and M. Kojima (2001), Improvements to the HAF solar wind model for space weather predictions, *J. Geophys. Res.*, *106*, 20,985–21,001, doi:10.1029/2000JA000220.

Gosling, J. T. (1990), Coronal mass ejections and magnetic flux ropes in interplanetary space, in *Physics of Magnetic Flux Ropes*, *Geophys. Monogr. Ser.*, vol. 58, edited by C. T. Russell, E. R. Priest, and L. C. Lee, pp. 343–364, AGU, Washington, D. C.

Guhathakurta, M., T. E. Holzer, and R. M. MacQueen (1996), The large-scale density structure of the solar corona and the heliospheric current sheet, *Astrophys. J.*, *458*, 817–831, doi:10.1086/176860.

Hayashi, K. (2005), Magnetohydrodynamic simulations of the solar corona and solar wind using a boundary treatment to limit solar wind mass flux, *Astrophys. J.*, *161*, 480–494, doi:10.1086/491791.

Hayashi, K., X. P. Zhao, and Y. Liu (2006), MHD simulation of two successive interplanetary disturbances driven by cone-model parameters in IPS-based solar wind, *Geophys. Res. Lett.*, *33*, L20103, doi:10.1029/2006GL027408.

Lugaz, N., and I. I. Roussev (2010), Numerical modeling of interplanetary coronal mass ejections and comparison with heliospheric images, *J. Atmos. Sol. Terr. Phys.*, *73*, 1187–1200, doi:10.1016/j.jastp.2010.08.016.

Lugaz, N., W. B. Manchester IV, and T. I. Gombosi (2005), Numerical simulation of the interaction of two coronal mass ejections from Sun to Earth, *Astrophys. J.*, *634*, 651–662, doi:10.1086/491782.

Lugaz, N., W. B. Manchester IV, I. I. Roussev, G. Tóth, and T. I. Gombosi (2007), Numerical investigation of the homologous coronal mass ejection events from active region 9236, *Astrophys. J.*, *659*, 788–800, doi:10.1086/512005.

Manchester, W. B., IV, T. I. Gombosi, I. Roussev, D. L. De Zeeuw, I. V. Sokolov, K. G. Powell, G. Tóth, and M. Opher (2004), Three-dimensional MHD simulation of a flux rope driven CME, *J. Geophys. Res.*, *109*, A01102, doi:10.1029/2002JA009672.

McComas, D. J., B. L. Barraclough, H. O. Funsten, J. T. Gosling, E. Santiago-Muñoz, R. M. Skoug, B. E. Goldstein, M. Neugebauer, P. Riley, and A. Balogh (2000), Solar wind observations over Ulysses' first full polar orbit, *J. Geophys. Res.*, *105*, 10,419–10,433, doi:10.1029/1999JA000383.

McComas, D. J., H. A. Elliott, N. A. Schwadron, J. T. Gosling, R. M. Skoug, and B. E. Goldstein (2003), The three-dimensional solar wind around solar maximum, *Geophys. Res. Lett.*, *30*(10), 1517, doi:10.1029/2003GL017136.

McComas, D. J., H. A. Elliott, J. T. Gosling, and R. M. Skoug (2006), Ulysses observations of very different heliospheric structure during the declining phase of solar activity cycle 23, *Geophys. Res. Lett.*, *33*, L09102, doi:10.1029/2006GL025915.

Nakagawa, Y., Y. Q. Hu, and S. T. Wu (1987), The method of projected characteristics for the evolution of magnetic arches, *Astron. Astrophys.*, *179*, 354–370.

Odstrcil, D., and V. J. Pizzo (2009), Numerical heliospheric simulations as assisting tool for interpretation of observations by STEREO heliospheric imagers, *Sol. Phys.*, *259*, 297–309, doi:10.1007/s11207-009-9449-z.

Odstrcil, D., P. Riley, and X. P. Zhao (2004), Numerical simulation of the 12 May 1997 interplanetary CME event, *J. Geophys. Res.*, *109*, A02116, doi:10.1029/2003JA010135.

Schmidt, J., and P. Cargill (2004), A numerical study of two interacting coronal mass ejections, *Ann. Geophys.*, *22*, 2245–2254, doi:10.5194/angeo-22-2245-2004.

Shen, F., X. Feng, S. T. Wu, and C. Xiang (2007), Three-dimensional MHD simulation of CMEs in three-dimensional background solar wind with the self-consistent structure on the source surface as input: Numerical simulation of the January 1997 Sun-Earth connection event, *J. Geophys. Res.*, *112*, A06109, doi:10.1029/2006JA012164.

Shen, F., X. Feng, and W. B. Song (2009), An asynchronous and parallel time-marching method: Application to the three-dimensional MHD simulation of the solar wind, *Sci. China Ser. E, Tech. Sci.*, *52*, 2895–2902.

Shen, F., X. Feng, C. Xiang, and W. B. Song, (2010), The statistical and numerical study of the global distribution of coronal plasma and magnetic field near 2.5 R_s over a 10-year period, *J. Atmos. Sol. Terr. Phys.*, *72*, 1008–1018, doi:10.1016/j.jastp.2010.05.016.

Shen, F., X. Feng, S. T. Wu, C. Xiang, and W. B. Song (2011), Three-dimensional MHD simulation of the evolution of the April 2000 CME event and its induced shocks using a magnetized plasma blob model, *J. Geophys. Res.*, *116*, A04102, doi:10.1029/2010JA015809.

Tóth, G. (2000), The $\nabla \cdot \vec{B} = 0$ constraint in shock-capturing magnetohydrodynamics codes, *J. Comput. Phys.*, *161*, 605–652.

Wang, Y., H. Zheng, S. Wang, and P. Ye (2005), MHD simulation of the formation and propagation of multiple magnetic clouds in the heliosphere, *Astron. Astrophys.*, *434*, 309–316, doi:10.1051/0004-6361:20041423.

Wang, Y. M., S. Wang, and P. Z. Ye (2002), Multiple magnetic clouds in interplanetary space, *Sol. Phys.*, *211*, 333–344, doi:10.1023/A:1022404425398.

Wang, Y. M., P. Z. Ye, and S. Wang (2003), Multiple magnetic clouds: Several examples during March–April 2001, *J. Geophys. Res.*, *108*(A10), 1370, doi:10.1029/2003JA009850.

Wang, Y. M., P.-Z. Ye, and S. Wang (2004), An interplanetary origin of great geomagnetic storms: Multiple magnetic clouds, Chin. *J. Geophys.*, *47*, 369–375.

Wei, F., X. Feng, H. Cai, and Q. Zhou (2003), Global distribution of coronal mass outputs and its relation to solar magnetic field structures, *J. Geophys. Res.*, *108*(A6), 1238, doi:10.1029/2002JA009439.

Wu, C.-C., C. D. Fry, M. Dryer, S. T. Wu, B. Thompson, K. Liou, and X. S. Feng (2007), Three-dimensional global simulation of multiple ICMEs interaction and propagation from the Sun to the heliosphere following the 25–28 October 2003 solar events, *Adv. Space Res.*, *40*, 1827–1834, doi:10.1016/j.asr.2007.06.025.

Wu, S. T., and J. F. Wang (1987) Numerical tests of a modified full implicit Eulerian scheme with projected normal characteristic boundary conditions for MHD flows, *Comput. Methods Appl. Mech. Eng.*, *24*, 267–282.

Wu, S. T., W. P. Guo, D. J. Michels, and L. F. Burlaga (1999), MHD description of the dynamical relationships between a flux rope, streamer, coronal mass ejection, and magnetic cloud: An analysis of the January 1997 Sun-Earth connection event, *J. Geophys. Res.*, *104*, 14,789–14,801, doi:10.1029/1999JA900099.

Wu, S. T., A. H. Wang, and N. Gopalswamy (2002), MHD modeling of CME and CME interactions in a bi-model solar wind: A preliminary analysis of the 20 January 2001 two CMES interaction event, *Eur. Space Agency Spec. Publ.*, *ESA SP-505*, 227–230.

Wu, S. T., A. H. Wang, Y. Liu, and J. T. Hoeksema (2006), Data-driven magnetohydrodynamic model for active region evolution, *Astrophys. J.*, *652*, 800–811, doi:10.1086/507864.

Xiang, C. Q., X. S. Feng, Q. L. Fan, and J. S. Yao (2006), An observation-based model of solar wind background, *Chin. J. Space Sci.*, *26*, 161–166.

Xiong, M., H. Zheng, Y. Wang, and S. Wang (2006a), Magnetohydrodynamic simulation of the interaction between interplanetary strong shock and magnetic cloud and its consequent geoeffectiveness, *J. Geophys. Res.*, *111*, A08105, doi:10.1029/2005JA011593.

Xiong, M., H. Zheng, Y. Wang, and S. Wang (2006b), Magnetohydrodynamic simulation of the interaction between interplanetary strong shock and magnetic cloud and its consequent geoeffectiveness: 2. Oblique collision, *J. Geophys. Res.*, *111*, A11102, doi:10.1029/2006JA011901.

Xiong, M., H. Zheng, S. T. Wu, Y. Wang, and S. Wang (2007), Magnetohydrodynamic simulation of the interaction between two interplanetary magnetic clouds and its consequent geoeffectiveness, *J. Geophys. Res.*, *112*, A11103, doi:10.1029/2007JA012320.

Xiong, M., H. Zheng, and S. Wang (2009), Magnetohydrodynamic simulation of the interaction between two interplanetary magnetic clouds and its consequent geoeffectiveness: 2. Oblique collision, *J. Geophys. Res.*, *114*, A11101, doi:10.1029/2009JA014079.

Zhao, X. P., and J. T. Hoeksema (1994), A coronal magnetic field model with horizontal volume and sheet current, *Sol. Phys.*, *151*, 91–105.

Zhou, Y. F., and X. S. Feng (2008), Numerical study of successive CMEs during November 4–5, 1998, *Sci. China Ser. E, Tech. Sci.*, *51*, 1–11.

X. S. Feng, J. P. Guo, F. Shen, W. B. Song, and Y. F. Zhou, SIGMA Weather Group, State Key Laboratory of Space Weather, Center for Space Science and Applied Research, Chinese Academy of Sciences, Beijing 100190, China. (fshen@spaceweather.ac.cn)

Y. Wang, School of Earth and Space Sciences, University of Science and Technology of China, Hefei, Anhui 230026, China.

S. T. Wu, Center for Space Plasma and Aeronomic Research, University of Alabama in Huntsville, Huntsville, AL 35899, USA.